INTERNATIONAL JOURNAL FOR NUMERICAL METHODS IN FLUIDS
Int. J. Numer. Meth. Fluids 2005; **49**:1087–1110

A combined vortex and panel method for numerical simulations of viscous flows: a comparative study of a vortex particle method and a finite volume method

Kwang-Soo Kim[1,*,†], Seung-Jae Lee[2] and Jung-Chun Suh[2,‡]

[1] *Korea Research Institute of Ships and Ocean Engineering, KORDI, Jang-dong 171, Yusong-gu, DaeJeon 305-343, South Korea*
[2] *Department of Naval Architecture and Ocean Engineering, College of Engineering, Seoul National University, San 56-1, Shillim-dong, Kwanak-gu, Seoul 151-742, South Korea*

SUMMARY

This paper describes and compares two vorticity-based integral approaches for the solution of the incompressible Navier–Stokes equations. Either a Lagrangian vortex particle method or an Eulerian finite volume scheme is implemented to solve the vorticity transport equation with a vorticity boundary condition. The Biot–Savart integral is used to compute the velocity field from a vorticity distribution over a fluid domain. The vorticity boundary condition is improved by the use of an iteration scheme connected with the well-established panel method. In the early stages of development of flows around an impulsively started circular cylinder, and past an impulsively started foil with varying angles of attack, the computational results obtained by the Lagrangian vortex method are compared with those obtained by the Eulerian finite volume method. The comparison is performed separately for the pressure fields as well. The results obtained by the two methods are in good agreement, and give a better understanding of the vorticity-based methods. Copyright © 2005 John Wiley & Sons, Ltd.

KEY WORDS: vorticity-velocity-pressure formulation; panel method; Eulerian finite volume method; Lagrangian vortex method; impulsively started cylinder; impulsively started foil

---

[*] Correspondence to: Kwang-Soo Kim, Korea Research Institute of Ships and Ocean Engineering, KORDI, Jang-dong 171, Yusong-gu, DaeJeon 305-343, South Korea.
[†] E-mail: ksookim@kriso.re.kr
[‡] E-mail: jungsuh@snu.ac.kr

Contract/grant sponsor: The Ministry of Science and Technology, Korea; contract/grant numbers: PN00630, PN00690
Contract/grant sponsor: Korea Science and Engineering Foundation; contract/grant number: R11-2002-104-02002-0

Received 24 August 2004
Revised 8 April 2005
Accepted 21 April 2005

1. INTRODUCTION

The Lagrangian vortex method is based on the discretization of the vorticity field: its main idea is the application of the particle method in vortex flow. This 'gridless method' is very attractive for numerical simulations of viscous flow around a body with complex geometry. It is then possible to avoid the nonlinear convection term of the vorticity transport equation, which involves difficulties associated with numerical diffusion for its discretization in grid-based methods. In fact, the Lagrangian vortex method has been used in earlier research for the computation of high-resolution simulations of viscous flows with solid boundaries: fast algorithms using multipole expansions [1], treatment of viscous diffusion using the particle strength exchange scheme (refer to 'PSE scheme' below) [2], and enforcement of the no-slip boundary condition [3, 4]. A thorough review of the foundation of the method and an extensive account of its previous applications may be found in several studies [5–10].

In the case of the vorticity-velocity formulation, there are some advantages over the primitive variable formulation. In externally attached flow problems, where the viscous region occupies only the boundary layer and wake, a computational region for vorticity evolution can be confined to this region of the entire flow field [11]. Furthermore, the use of the vorticity field may be suitable in the study of certain features of established vortical flows. One of the most difficult problems encountered in the vorticity-velocity formulation is the introduction of the proper value of vorticity or vorticity flux at the solid surface [12]. The fluid around a solid body may presumably appear at any instant in time to have a spurious slip velocity component on the surface of the solid body. This apparent slip velocity must be reduced to zero by the production of a proper quantity of vorticity at the surface. This vorticity then enters and is distributed throughout the fluid by convection and diffusion. This distribution of the vorticity is governed by the vorticity transport equation. Wu *et al.* [13] presented a systematic theoretical analysis for these dynamic boundary conditions. They proposed a fully decoupled scheme based on fractional step methods (in which the vorticity transport equation is separated into convection and diffusion equations) applicable for high Reynolds numbers. In the work of Koumoutsakos and Leonard [14], a fractional two-step algorithm is employed in a similar way to the work of Wu *et al.* In the first step, vortex particles are convected during a time interval with velocities computed via the Biot–Savart integral with a smoothed kernel. Their strengths are modified based on the PSE. In the second step, a spurious slip velocity, which is computed on the surface of a body at the end of the first step, is related to a vorticity flux generating from the solid wall in the fluid.

In a previous study [15], we proposed a similar concept based on an integro-differential formulation for the solution of unsteady incompressible Navier–Stokes equations. The distinctive feature was the use of an integral approach for obtaining the velocity and pressure fields, in conjunction with a finite volume scheme for solving the vorticity transport equation.

The present work revisits an integral approach to the vorticity-velocity-pressure formulation and gives a comparative study of numerical solutions obtained by two vorticity-based formulations: an Eulerian finite volume method and a Lagrangian vortex method. The integral approaches for obtaining the velocity and pressure fields are expected to reflect more effectively the global coupling among vorticity, velocity and pressure when imposing the boundary condition for vorticity at a solid surface. A mathematical identity for a vector or scalar field is used to define field values of a quantity of interest, which involves an integral of singularities distributed over the surface and throughout the field. This concept has been well established for potential flow analysis and has been extensively used to solve viscous flow problems (see Reference [16] for general description). In this regard, we introduce a mixed scheme as a combination of the existing vortex methods and the panel method [17, 18]. The velocity field of the external flow is based on the Helmholtz decomposition: $\mathbf{u} = \mathbf{u}_\infty + \mathbf{u}_w + \nabla\phi$, where $\mathbf{u}_\infty$ is an undisturbed velocity, and $\mathbf{u}_w$ represents a rotational field. The contribution of the velocity component of the potential flow $\nabla\phi$ is not only physically natural, but also helpful in considering the kinematics of flow: e.g. the no-penetration condition and the divergence-free constraint of vorticity. The present work deals with the pressure calculation as well, which has not been treated in most vorticity-based methods.

In the context of the numerical implementation, the no-slip boundary condition is enforced by assigning the vorticity flux at the solid surface. The vorticity flux at the surface is assigned as its time-averaged value during a small time interval (Δt). In this stage, we propose an iterative process to introduce a proper amount of the time-averaged vorticity flux in order to ensure the no-slip condition. Also, in order to complete the PSE scheme of the vortex method in the presence of boundaries, we use an 'image particle layer' inside the boundaries. The image particle layer reflects an overall effect of all vortex particles in the field on the presence of the boundaries [19].

For a comparative study, we take an impulsively started circular cylinder problem and an impulsively started NACA0021 foil with varying angles of attack, in which certain special features are apparent, notably concerning the vorticity distribution on the surfaces. Our numerical results could be judged by a comparison with the existing analytical solution provided by Bar-Lev and Yang [20], in the case of the cylinder, and with the results of the previous work using the finite volume method [15].

2. BASIC FORMULATION

The stress tensor for incompressible Newtonian fluids can be expressed as

$$\sigma_{ij} = -p\delta_{ij} + \mu\left(\frac{\partial u_i}{\partial x_j} + \frac{\partial u_j}{\partial x_i}\right) \tag{1}$$

and the stress vector, with the normal vector $\mathbf{n}$, is written as

$$\boldsymbol{\tau} = -p\mathbf{n} + \mu\boldsymbol{\omega} \times \mathbf{n} + 2\mu\nabla\mathbf{u} \cdot \mathbf{n} \tag{2}$$

where $\mathbf{u}, \boldsymbol{\omega}$ and p are the velocity, the vorticity and the pressure, respectively. The last term of the equation gives no net contribution to fluid surface forces. Thus, the Navier–Stokes equations can be represented, ignoring any external body forces, as

$$-\rho\frac{\mathrm{d}\mathbf{u}}{\mathrm{d}t} = \nabla p + \nabla \times \mu\boldsymbol{\omega} \tag{3}$$

where μ is viscosity and ρ density (set to $\rho = 1$ for simplicity). Equation (3) is of a Helmholtz decomposition form, p and $\mu\boldsymbol{\omega}$ being a pair of the potential forces.

The governing equations for the unsteady flow of a Newtonian incompressible fluid are written as

$$\nabla \cdot \mathbf{u} = 0 \tag{4}$$

$$\boldsymbol{\omega} = \nabla \times \mathbf{u} \tag{5}$$

$$\frac{\partial \boldsymbol{\omega}}{\partial t} + \mathbf{u} \cdot \nabla \boldsymbol{\omega} = \boldsymbol{\omega} \cdot \nabla \mathbf{u} + \nu \nabla^2 \boldsymbol{\omega} \tag{6}$$

$$\nabla^2 \left(\frac{p}{\rho} + \frac{1}{2} u^2 \right) = \nabla \cdot (\mathbf{u} \times \boldsymbol{\omega}) \tag{7}$$

The set of Equations (5)–(7) is one of the basic differential vorticity-velocity formulations. Note that a Poisson equation for the velocity, $\nabla^2 \mathbf{u} = -\nabla \times \boldsymbol{\omega}$, is often used to replace Equation (5). Some research on vortex methods deals with the vorticity-streamfunction formulation instead.

According to the mathematical vector identity, an equivalent integral formulation of Equation (5) is written, with use of Equation (4), as

$$\mathbf{u} = \int_S [(\mathbf{n} \cdot \mathbf{u}) \nabla G + (\mathbf{n} \times \mathbf{u}) \times \nabla G] \, \mathrm{d}S + \int_V \boldsymbol{\omega} \times \nabla G \, \mathrm{d}V \tag{8}$$

where **n** is the unit normal pointing into the fluid at the boundary S (C in 2-dimensions) of a fluid domain V (S in 2-dimensions) and ∇ denotes the differential operator with respect to the variable of integration $\boldsymbol{\xi}$. Here, G is the fundamental solution of the Laplace equation for an unbounded fluid domain, which is defined by $G = 1/4\pi r$ in 3-dimensions and $G = -1/2\pi \ln r$ in 2-dimensions, where r is the distance between a field point $\mathbf{x}$ and an integration point $\boldsymbol{\xi}$. The first integral of Equation (8) represents the contribution from the undisturbed onset flows ($\mathbf{u}_\infty$) and the potential flows ($\nabla \phi$). The second integral, known as the Biot–Savart law, represents the disturbance velocity field ($\mathbf{u}_\omega$) induced by a vorticity field. Using the Biot–Savart law in computing the velocity field guarantees the enforcement of the boundary condition for the velocity at infinity.

Similarly, an integral formulation of Equation (7) can be written as

$$H = \int_S \left[H \frac{\partial G}{\partial n} - \frac{\partial H}{\partial n} G \right] \mathrm{d}S + \int_V \nabla \cdot (\mathbf{u} \times \boldsymbol{\omega}) G \, \mathrm{d}V \tag{9}$$

Here, the pressure p is related to the total pressure H (the static plus the dynamic pressure) defined by

$$H = \frac{p - p_\infty}{\rho} + \frac{1}{2} (u^2 - u_\infty^2) \tag{10}$$

where the constants p_∞ and u_∞ are the reference pressure and velocity at infinity (or at a reference point), respectively. With this definition, the boundary condition at infinity for H is expressed by $H \to 0$ as $|\mathbf{x}| \to \infty$. Thus, the contribution due to H at infinity is not considered when solving Equation (9).

The system of Equations (6), (8) and (9) are solved in the fluid domain with boundary conditions for velocity, vorticity and pressure on the surface (C_B) of a solid body. The no-slip velocity condition states that the velocity of the fluid ($\mathbf{u}$) is equal to the velocity of the body ($\mathbf{U}_\mathrm{B}$) at the surface points ($\mathbf{x}_\mathrm{B}$) of the body:

$$\mathbf{u}(\mathbf{x}_\mathrm{B}, t) = \mathbf{U}_\mathrm{B} \quad \text{on } C_\mathrm{B}$$

The boundary vorticity flux at the solid body is

$$\nu \frac{\partial \boldsymbol{\omega}}{\partial n} = \left(\mathbf{n} \times \frac{\mathrm{d}\mathbf{U}_{\mathrm{B}}}{\mathrm{d}t} + \mathbf{n} \times \nabla \frac{p}{\rho} \right) \quad \text{on } C_{\mathrm{B}} \tag{11}$$

This essential boundary condition for the vorticity at the solid surface can be derived by taking the cross product of the Navier–Stokes equations (Equation (3)) with **n**, under the velocity adherence condition. This condition corresponds to the force equilibrium in the direction tangent to the solid surface. This represents an explicit expression of the process of vorticity production described qualitatively by Lighthill [21]. This quantity of the vorticity flux diffuses into the fluid from the body surface. The above expression applies to $t = 0^{+}$ as well and is, therefore, applicable immediately after a solid body is accelerated impulsively. Similarly, the scalar product of the Navier–Stokes equations (Equation (3)) with **n** gives an expression for $\partial H/\partial n$ as:

$$\frac{\partial H}{\partial n} = -\,\mathbf{n} \cdot \frac{\partial \mathbf{u}}{\partial t} + \mathbf{n} \cdot (\mathbf{u} \times \boldsymbol{\omega}) - \mathbf{n} \cdot (\nabla \times \nu \boldsymbol{\omega}) \quad \text{on } C_{\mathrm{B}} \tag{12}$$

From Equations (11) and (12), we can see that the boundary conditions for the vorticity and the pressure are coupled. A more rigorous and extensive analysis of these pressure and vorticity conditions for the two- or three-dimensional incompressible or compressible flows was given by Wu and Wu [22].

In the previous study [15], the authors presented a numerical method using an integral approach for obtaining the velocity and pressure fields, in conjunction with a finite volume method for solving the vorticity transport equation.

In a finite volume discretization applied to Equation (6), integrating the vorticity transport equation over an arbitrary but stationary cell, and then applying the divergence theorem, yields an integral form. In this integral form of the vorticity transport equation, the diffusive flux term was approximated in a similar fashion to the central difference scheme. For the convection term, the second-order total variation diminishing (TVD) scheme with a flux limiter was used. Time was advanced by an explicit forward Euler time-stepping scheme with time interval Δt. The velocity field was calculated by the direct evaluation of the Biot–Savart integral, Equation (8) from the transformation of the involved integrands. Applying the Gauss integral theorem for the transformed integrals reduces the surface integrals to the line integrals, being rendered in terms of the closed form of the line integrals along the boundary of an individual cell. For the pressure fields, Equation (9) was solved using a panel method approximation. For the boundary conditions with global coupling of vorticity, velocity and pressure, the iteration scheme was used. See References [15, 19, 23] for more details.

3. LAGRANGIAN VORTEX METHOD

In the case of two-dimensional flows, a Lagrangian form of Equation (6) is represented as

$$\frac{D\omega}{Dt} = \nu \nabla^{2} \omega \tag{13}$$

where ω is the scalar plane component of the vorticity vector ($\boldsymbol{\omega} \equiv \omega\mathbf{k}$). The vorticity field in two-dimensional flows is represented by N scalar-valued particles:

$$\omega(\mathbf{x}, t) = \sum_{i=1}^{N} \varphi_i(\mathbf{x} - \mathbf{x}_i)\Gamma_i \tag{14}$$

Each particle is characterized by its position, $\mathbf{x}_i(t)$, and its strength, $\Gamma_i(t)$, i.e. its circulation, $\Gamma_i = \int_{S_i} \omega \, \mathrm{d}S \approx \omega_i S_i$, with S_i the area of fluid associated with the particle i. The regularized particle representation of the vorticity field has been used by various researchers [6, 24, 25]. The distribution functions φ_i associated with each particle are defined by

$$\varphi_i(\mathbf{x}) = \frac{1}{\varepsilon_i^2} \varphi\left(\frac{|\mathbf{x}|}{\varepsilon_i}\right) \tag{15}$$

where ε_i is the smoothing parameter denoting the blob (particle) size. In the present study, we choose Gaussian smoothing as the distribution function for its physically appealing properties:

$$\varphi(\rho) = \frac{1}{2\pi} \exp\left(-\frac{\rho^2}{2}\right) \tag{16}$$

3.1. Velocity calculation

Vortex particle positions $\mathbf{x}_i(t)$ are governed by the equation,

$$\frac{\mathrm{d}\mathbf{x}_i}{\mathrm{d}t} = \mathbf{u}(\mathbf{x}_i, t) = \mathbf{u}_\infty + \nabla\phi + \mathbf{u}_\omega \tag{17}$$

The velocity at any position $\mathbf{x}$ in Equation (17) in the Lagrangian description can be calculated by using Equations (8) and (14). The first term of the closed integral term in Equation (8) may be calculated by the well-established panel method in a similar fashion to the analysis of the potential flow. According to Green's scalar identity, the potential ϕ at arbitrary points on the body surface is written as

$$\frac{1}{2}\phi(\mathbf{x}) = \oint \phi(\mathbf{y})\mathbf{n}(\mathbf{y}) \cdot \nabla G(\mathbf{x} - \mathbf{y}) + \mathbf{n}(\mathbf{y}) \cdot \nabla\phi(\mathbf{y}) G(\mathbf{x} - \mathbf{y}) \, \mathrm{d}l_y \tag{18}$$

Assume that a density distribution of singularity strength on each panel at the boundary (subdivided into M) is uniform. The integral equation of Equation (18) is discretized as

$$\frac{1}{2}\phi_i(\mathbf{x}) = \sum_{j=1}^{M} A_{ij}\phi_j + \sum_{j=1}^{M} B_{ij}\sigma_j$$

where $\mathbf{n} \cdot \nabla\phi_j = -\mathbf{n} \cdot (-\mathbf{U}_\mathrm{B} + \mathbf{u}_\infty + \mathbf{u}_\omega) = \sigma_j, A_{ij} = \int_{C_j} \mathbf{n}(\mathbf{y}) \cdot \nabla G \, \mathrm{d}l_y, B_{ij} = \int_{C_j} G \, \mathrm{d}l_y$. Since the source strength σ_j is a known value, the line integrals for each panel, A_{ij}, B_{ij} can be solved algebraically [23]. While $\nabla\phi$ on the body surface can be approximated in the sense of the finite difference of ϕ_i, $\nabla\phi$ at field points can be computed as

$$\nabla\phi(\mathbf{x}) = \frac{1}{2\pi} \oint_S \left[\phi(\mathbf{y}) \left(\frac{\mathbf{n}(\mathbf{y})}{r^2} - 2\frac{\mathbf{n}(\mathbf{y}) \cdot \mathbf{r}}{r^4}\mathbf{r}\right) + \mathbf{n}(\mathbf{y})\nabla\phi(\mathbf{y})\frac{\mathbf{r}}{r^2}\right] \mathrm{d}S_y \tag{19}$$

where $\mathbf{r}=\mathbf{x}-\mathbf{y}$. The irrotational part of the velocity field ($\nabla\phi$) obtained by the panel method compensates the kinematics of particles in such a manner that the no-penetration condition (e.g. $\mathbf{u}\cdot\mathbf{n}=\mathbf{U}_{\mathrm{B}}\cdot\mathbf{n}$) applies (see References [17, 18] for panel method).

The second term of the Biot–Savart integral in Equation (8) may be discretized by the Lagrangian vorticity field, Equation (14) as

$$\mathbf{u}_{\omega}(\mathbf{x},t)=-\frac{1}{2\pi}\sum_{i=1}^{N}\mathbf{K}_{\sigma}\times\Gamma_i(\mathbf{x}_i)\mathbf{k} \tag{20}$$

where $R=|\mathbf{x}-\mathbf{x}_i|, \mathbf{K}=(\mathbf{x}-\mathbf{x}_i)/|\mathbf{x}-\mathbf{x}_i|^2, \mathbf{K}_{\varepsilon}=\mathbf{K}\{1-\exp(-|R|^2/2\varepsilon^2)\}$. In order to obtain the spurious slip velocity (V_{s}) on the body surface, a field point $\mathbf{x}$ is replaced by $\mathbf{x}_{\mathrm{B}}$ on the body panel. We compute Equation (20) using a fast algorithm [1] with an operation count of $\mathcal{O}(N\log(N))$ rather than $O(N^2)$.

3.2. *Viscous diffusion*

The treatment of the diffusion equation (Equation (13)) is based on a technique related to the PSE scheme introduced by Degond and Mas-Gallic [2]. The Laplacian operator ∇^2 is approximated by an integral operator, which is discretized over the particles.

$$v\nabla^2\omega\approx\frac{2v}{\varepsilon^2}\int_{\Omega}\eta_{\varepsilon}(|\mathbf{x}-\mathbf{y}|)(\omega(\mathbf{y})-\omega(\mathbf{x}))\,\mathrm{d}\mathbf{y} \tag{21}$$

Then, the evolution equation for the particle strengths becomes

$$\frac{\mathrm{d}\Gamma_i}{\mathrm{d}t}=\frac{2v}{\varepsilon^2}\sum_{j=1}^{N}(S_i\Gamma_j-S_j\Gamma_i)\eta_{\varepsilon}(\mathbf{x}_i-\mathbf{x}_j) \tag{22}$$

where $\eta_{\varepsilon}(\mathbf{x}_i-\mathbf{x}_j)=1/(2\pi\varepsilon^2)\exp(-|\mathbf{x}_i-\mathbf{x}_j|^2/2\varepsilon^2)$ being the same as Equation (16). Herein, ε is constant for all particles. If Equation (22) is used for wall-bounded computations, particles close to the wall are not completely surrounded by other particles. Consequently, a spurious vorticity flux appears at the wall while the total vorticity is conserved [4, 10].

We use an image particle layer to complete the PSE for particles close to the wall. Solid walls are approximated as discretized panels. The images are placed along a layer inside the body close to the panel, as shown in Figure 1. The extended vorticity of the image layer adds to the vorticity on the body,

$$\boldsymbol{\omega}(\mathbf{x})=\sum_{i=1}^{N}\Gamma_i\varphi_i(\mathbf{x}-\mathbf{x}_i)+\sum_{m=1}^{M}\Gamma_m^*\varphi_m^*(\mathbf{x}-\mathbf{x}_m^*)\quad \mathbf{x}\in\partial\mathscr{D} \tag{23}$$

where the superscript '$*$' refers to quantities of images. Then the vorticity flux on the body is expressed as

$$\frac{\partial\boldsymbol{\omega}}{\partial\mathbf{n}}=\sum_{i=1}^{N}\Gamma_i\frac{\partial\varphi_i}{\partial\mathbf{n}}(\mathbf{x}-\mathbf{x}_i)+\sum_{m=1}^{M}\Gamma_m^*\frac{\partial\varphi_m^*}{\partial\mathbf{n}}(\mathbf{x}-\mathbf{x}_m^*)\quad \mathbf{x}\in\partial\mathscr{D} \tag{24}$$

where $\mathbf{n}$ is the normal vector of the particle $\mathbf{x}$ and the zero-vorticity-flux condition means $\partial\boldsymbol{\omega}/\partial\mathbf{n}=0$ at the body surface. The normal derivative of the smoothing function is

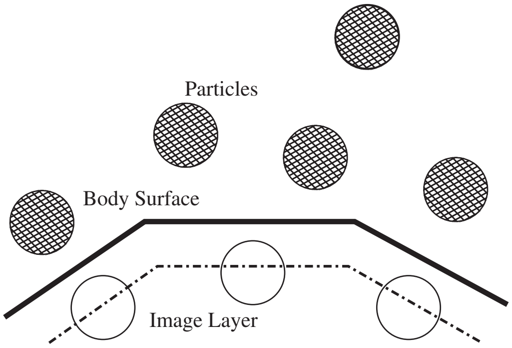

Figure 1. Image particle layer to enforce the zero-vorticity-flux condition at the body surface in PSE scheme.

found to be

$$\frac{\partial \varphi_i(\mathbf{r})}{\partial \mathbf{n}} = -\frac{1}{2\pi\varepsilon^4}\exp\left(-\frac{\mathbf{r}^2}{2\varepsilon^2}\right)(\mathbf{r}\cdot\mathbf{n}) \tag{25}$$

Denoting the radius of the image blob by ε^*, Equation (24) is expressed as

$$\frac{\partial \boldsymbol{\omega}(\mathbf{x}_p)}{\partial \mathbf{n}} = \frac{1}{2\pi\varepsilon^{*4}}\sum_{m=1}^{M}\Gamma_m^*\exp\left(-\frac{\mathbf{r}^{*2}}{2\varepsilon^{*2}}\right)(\mathbf{r}^*\cdot\mathbf{n}) + \frac{1}{2\pi\varepsilon^4}\sum_{i=1}^{N}\Gamma_i\exp\left(-\frac{\mathbf{r}^2}{2\varepsilon^2}\right)(\mathbf{r}\cdot\mathbf{n}) = 0 \tag{26}$$

where $\mathbf{r} = \mathbf{x}_p - \mathbf{x}_i$ and $\mathbf{r}^* = \mathbf{x}_p - \mathbf{x}_m$. With the image layer, Equation (21) is replaced by

$$\frac{\mathrm{d}\Gamma_i}{\mathrm{d}t}\frac{1}{S_i} = \frac{2\nu}{\varepsilon^2}\sum_{j=1}^{N}\left[\frac{\Gamma_j}{S_j} - \frac{\Gamma_i}{S_i}\right]\eta_\varepsilon(|\mathbf{x}_i - \mathbf{x}_j|)S_j + \frac{2\nu}{\varepsilon^2}\sum_{m=1}^{M}\left[\frac{\Gamma_m^*}{S_m} - \frac{\Gamma_i}{S_i}\right]\eta_\varepsilon(|\mathbf{x}_i - \mathbf{x}_m|)S_m \tag{27}$$

where $S_m = \varepsilon^{*2}$ for the image. This technique is insensitive to the local shape of a body. That is, because one image layer in the body is used, it may be suitable in the case of a thin body, e.g. foils with cusped trailing edges.

A vorticity flux ($\nu(\partial\omega/\partial n)$) may be determined on the boundary in such a way that the no-slip condition is satisfied. Wu *et al.* [13] introduced a relation between a vorticity flux and spurious slip velocity (V_s). If a vorticity flux is constant over a small interval of time (Δt), the spurious slip velocity (V_s) that would appear at the end of the time step can be regarded as the coupling term corresponding to the tangential gradient of the surface pressure in Equation (11). The newly computed V_s, which can be obtained by the Biot–Savart integral, can then be used to absorb the coupling term and consequently to update a vorticity flux:

$$\left(\nu\frac{\partial\omega}{\partial n}\right)^{(k+1)} = \left(\nu\frac{\partial\omega}{\partial n}\right)^{(k)} + \left(\frac{V_\mathrm{s}}{\Delta t}\right)^{(k)} \tag{28}$$

Here, the superscript notation refers to the iterative step. The iteration continues until the no-slip condition is satisfied, i.e. until V_s reduces to a value within a preset allowance. Equation (28) indicates the total flux to be emitted into the flow for the diffusion process during a time Δt. This elegant decoupled scheme was introduced by Wu *et al.* [13], through which we can efficiently recover the global coupling between the vorticity and pressure boundary condition instead of the implementation of the fully coupled schemes.

The vorticity flux is distributed to neighbouring particles by discretizing the Green's integral for the inhomogeneous Neumann problem corresponding to the diffusion equation. For diffusion within the schemes to work properly, the spatial distribution of the particles must remain as uniform as possible. To re-mesh the distorted particles, we overlaid a uniform rectangular grid. This is necessary in order to accurately interpolate the current vorticity field onto the new grid of initially uniformly spaced particle location that replaces the distorted particle locations (as suggested by Ploumhans and Winckelmans [4]).

3.3. Pressure equation

Once the vorticity and the velocity fields are updated, the integral equation for the total pressure may be solved. Basically, the process for calculating the pressure in a Lagrangian frame is similar to one in an Eulerian frame. Substituting Equation (12) for $\partial H/\partial n$ into Equation (12) yields the limiting form for H as the field point approaches the surface points $(\mathbf{x}_\mathrm{B})$ of a solid body:

$$\frac{1}{2}H + \frac{1}{2\pi}\int_{C_\mathrm{B}} H\,\frac{\partial(\ln r)}{\partial n}\,\mathrm{d}l = -\frac{1}{2\pi}\int_{C_\mathrm{B}}\left[\mathbf{n}\cdot\frac{\partial\mathbf{u}}{\partial t} - \mathbf{n}\cdot(\mathbf{u}\times\boldsymbol{\omega}) + \mathbf{n}\cdot(\nabla\times\nu\boldsymbol{\omega})\right]\ln r\,\mathrm{d}l + \frac{1}{2\pi}\int_S \nabla\cdot(\mathbf{u}\times\boldsymbol{\omega})\ln r\,\mathrm{d}S \tag{29}$$

where the integrals over C_B are evaluated on the surface of a body in the sense of the Cauchy principal value integral. Using the vector operation for the integrand of the surface integral in Equation (29), namely, $\nabla\cdot(\mathbf{u}\times\boldsymbol{\omega})\ln r = \nabla\cdot(\mathbf{u}\times\boldsymbol{\omega}\ln r) - (\mathbf{u}\times\boldsymbol{\omega})\cdot\nabla\ln r$ and applying the divergence integral theorem to the resultant expression, yield a Fredholm integral equation of the second kind for H:

$$\frac{1}{2}H + \frac{1}{2\pi}\int_{C_\mathrm{B}} H\,\frac{\partial(\ln r)}{\partial n}\,\mathrm{d}l = -\frac{1}{2\pi}\int_{C_\mathrm{B}}\left[\mathbf{n}\cdot\frac{\partial\mathbf{u}}{\partial t} + \mathbf{n}\cdot(\nabla\times\nu\boldsymbol{\omega})\right]\ln r\,\mathrm{d}l - \frac{1}{2\pi}\int_S(\mathbf{u}\times\boldsymbol{\omega})\cdot\nabla(\ln r)\,\mathrm{d}S$$

Furthermore, if we assume that the body will be either fixed, or impulsively started, as in the test problem, the equation reduces to a simpler form:

$$\frac{1}{2}H + \frac{1}{2\pi}\int_{C_\mathrm{B}} H\,\frac{\partial(\ln r)}{\partial n}\,\mathrm{d}l = -\frac{1}{2\pi}\int_{C_\mathrm{B}} \nu\frac{\partial\omega_\mathrm{B}}{\partial s}\ln r\,\mathrm{d}l - \frac{1}{2\pi}\int_S(\mathbf{u}\times\boldsymbol{\omega})\cdot\nabla(\ln r)\,\mathrm{d}S \tag{30}$$

The two integrals over C_B in Equation (30) may be replaced by the sum of the individual integral form for the contribution of each straight-line body panel. This can then be solved using the panel method in a way similar to that used in potential flow analysis (as mentioned in Section 3.1). The surface integral term on the right-hand side of Equation (30) may be solved with distorted vorticity particles, unlike the well-aligned cell elements in an Eulerian description. The discretization of Equation (30) (except the last surface integral term) is expressed as

$$\frac{1}{2}H_i + \frac{1}{2\pi}\sum_{j=1}^{M} H_j \int_j \nabla \ln r \, \mathrm{d}l_j = -\frac{1}{2\pi}\sum_{j=1}^{M}\{\mathbf{n}\cdot(\nabla \times \nu\boldsymbol{\omega})_j\}\int_j \ln \mathrm{r} \, \mathrm{d}l_j - \frac{1}{2\pi}\int_S (\mathbf{u}\times\boldsymbol{\omega})\cdot\nabla \ln r \, \mathrm{d}s \qquad (31)$$

Body vorticities on the body panels may be calculated from the distribution function of Equation (14). The second term on the right-hand side of Equation (31) (source-like strength, $\mathbf{n}\cdot\nabla\times\nu\boldsymbol{\omega}$) is calculated by numerically differentiating the body vorticities in the tangential direction of the body surface panel. With the vorticity field of Equation (14), the last integral term in Equation (31) is discretized as

$$\begin{aligned}\frac{1}{2\pi}\int(\mathbf{u}\times\boldsymbol{\omega})\cdot\nabla \ln r \, \mathrm{d}s &= \frac{1}{2\pi}\sum_{i=1}^{N}\mathbf{u}_i \times (\Gamma_i \mathbf{k})\cdot\frac{\mathbf{r}}{|\mathbf{r}|^2}\int \varphi_i \, \mathrm{d}s \\ &= \frac{1}{2\pi}\sum_{i=1}^{N}\left[\frac{(x-x_i)u_y\Gamma_i - (y-y_i)u_x\Gamma_i}{|\mathbf{r}|^2}\right]\left[1-\exp\left(-\frac{|\mathbf{r}|^2}{2\sigma^2}\right)\right]\end{aligned} \qquad (32)$$

3.4. Computational procedure

As shown in Figure 2, the numerical implementation for two-dimensional Lagrangian formulation can be summarized in the following substeps of the solution of the system of governing equations. The overall procedure is similar to those of Koumoutsakos *et al.* [3] and Ploumhans *et al.* [4]. In the present method, however, the irrotational (potential field) part of the velocity field is calculated by using the well-established panel method and the iterative process is used for more physically suitable creation of vorticity flux in order to ensure the no-slip condition, which was taken on the previous vorticity-based method in the Eulerian description [15]. A typical time step, Δt, of the Lagrangian vortex method is divided into two substeps.

(i) The local velocity ($\mathbf{u} = \mathbf{u}_\omega + \nabla\phi + \mathbf{u}_\infty$) is computed as follows: $\mathbf{u}_\omega$ calculated by the Biot–Savart integral (Equation (20)), $\nabla\phi$ calculated by the panel method (Equations (18) and (19)). Then, the velocity is integrated with a second-order Adam–Bashforth scheme (or a second-order Runge–Kutta method immediately after the redistribution process is applied) to convect the particle. Their strengths are updated with the PSE scheme (Equation (27)) that is integrated with an Euler explicit scheme. Algorithmically, this step is expressed as

$$\mathbf{x}_i^{n+1} = \mathbf{x}_i^n + \Delta t\left(\tfrac{3}{2}\,\mathbf{u}_i(\mathbf{x}^n,\Gamma^n) - \tfrac{1}{2}\,\mathbf{u}_i(\mathbf{x}^{n-1},\Gamma^{n-1})\right) \qquad (33)$$

$$\Gamma_i^* = \Gamma_i^n + \Delta t \left.\frac{\mathrm{d}\Gamma_i}{\mathrm{d}t}\right|_{\mathrm{PSE}} (\mathbf{x}^n,\Gamma^n) \qquad (34)$$

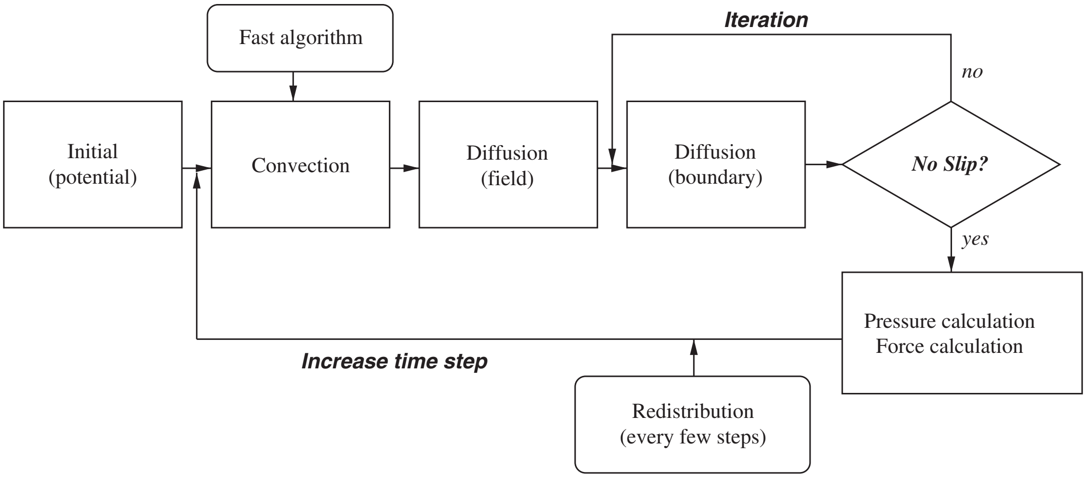

Figure 2. Numerical procedure of the Lagrangian vortex method.

(ii) The vorticity flux($\nu(\partial\omega/\partial n)$) necessary on the body surface to cancel the slip velocity computed by substep (i), is computed (Equation (20)). However, recalculation of the slip velocity on the body boundary may reveal that the no-slip condition is not satisfied. Vorticity flux due to the remaining slip velocity is then re-calculated. The iteration continues until the no-slip condition is satisfied, i.e. until the spurious slip velocity reduces to a value within a preset allowance. The vorticity strength corresponds to a vorticity flux that must be emitted during a time Δt:

$$\Gamma_i^{n+1} = \Gamma_i^* + \Delta t \left.\frac{\mathrm{d}\Gamma_i}{\mathrm{d}t}\right|_{\text{wall}} (\mathbf{x}^{n+1}, \Gamma^*) \tag{35}$$

The redistribution scheme is applied every few steps (herein every 5–10 time steps) to maintain spatial uniformity of the particle distribution. Once the vorticity and velocity are updated after two substeps are taken, the pressure equation (i.e. Equations (31) and (32)), is solved.

4. SOME COMPARATIVE RESULTS

4.1. Impulsively started cylinder

The time development of an incompressible viscous flow around an impulsively started circular cylinder is a classical problem in fluid mechanics. Despite the simplicity of its geometry, the flow structure is complicated and all possible flow phenomena occur [26]. In this section, comparative studies of this problem are performed with the results of the Eulerian formulation [15] and other researchers' work, including theoretical [20], and numerical [4, 14] investigations of the validity of the Lagrangian formulation.

Input parameters for the present comparison are as follows: $Re = U_\infty D/\nu = 550, T = tU_\infty/D$, $\Delta t = 0.05$, blob size $\varepsilon = 0.005$, surface panel size $d = \pi/600 \approx 0.0052$. These parameters are

Table I. Computational parameters used in the impulsively started cylinder problem.

	FVM	Vortex method
Reynolds number	550	550
Time step, Δt	0.01	0.01
Radius	0.5	0.5
Number of surface panels	600	600
Panel size	About 0.005	About 0.005
Grid meshes	600 × 40	—
Particles	—	9000–70 000
Computational domain	Diameter × 2.5	No limit
Computational time (Pentium IV)	About 6 h (400 time steps)	About 8 h (400 time steps)

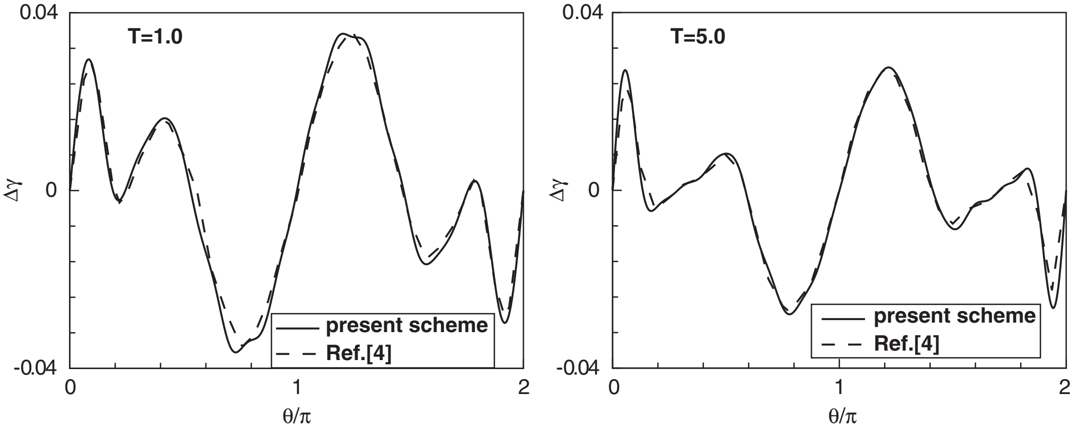

Figure 3. Comparison of the accumulated spurious slip velocity distribution on the cylinder surface; solid line (–), Lagrangian vortex method (present scheme); dashed line (– –), Lagrangian vortex method [4].

chosen to satisfy the stability condition $v\Delta t/h^2 = \mathcal{O}(1)$ for the diffusion term, and to satisfy the stability conditions of the second-order Adam–Bashforth scheme for the convection term, and the explicit Euler scheme for time marching. N particles (or blobs) result in the so-called 'N-body problem' in the evaluation of the Biot–Savart integral. Therefore, the convection and diffusion terms are treated with the fast algorithm [1] to reduce computing time. Computational parameters used for the present comparison are tabulated in Table I.

Figure 3 gives the comparison of vortex sheet strength with the results by Ploumhans and Winckelmans [4]. The vortex sheet strength ($\Delta\gamma$) is equivalent to the accumulation of spurious slip velocity on the body boundary, which is calculated during the iterative process for the no-slip condition. The results of Ploumhans and Winckelmans are obtained in a manner such that vortex singularities are distributed on the body surfaces, and the no-slip condition is conferred to the interior boundary surfaces, which is equivalent to a no-penetration condition. Figure 3 shows that the distribution of $\Delta\gamma$ is in good agreement, except for some peak values.

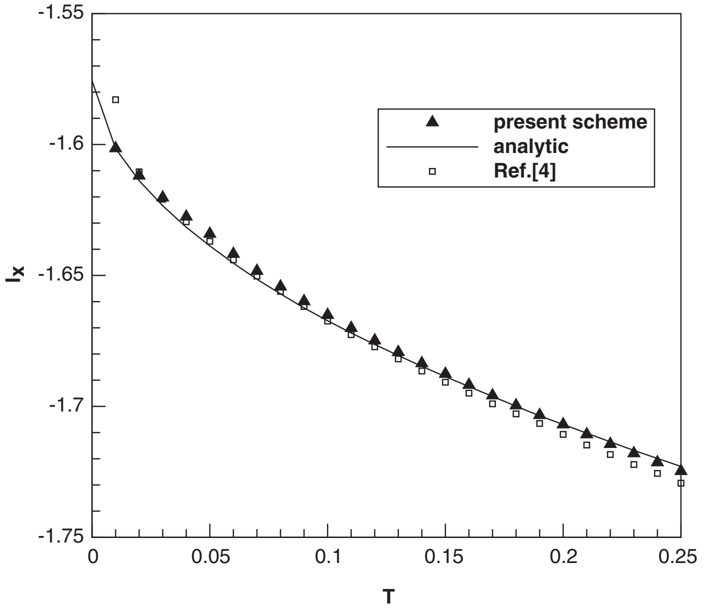

Figure 4. I_x comparison for the impulsively started cylinder problem ($0<T<0.25$): solid line ($-$), analytical [20]; ▲, Lagrangian vortex method (present scheme); □, Lagrangian vortex method [4].

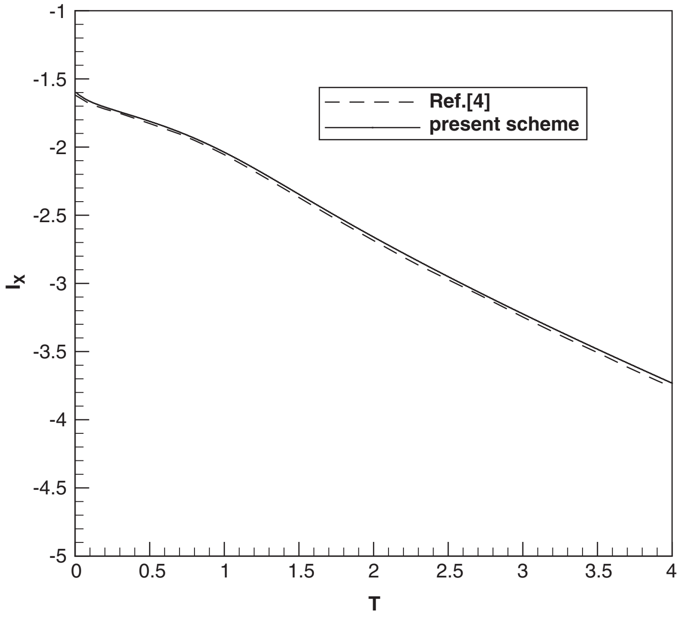

Figure 5. I_x comparison for the impulsively started cylinder problem ($0<T<4$): solid line ($-$), Lagrangian vortex method (present scheme); dashed line ($--$), Lagrangian vortex method [4].

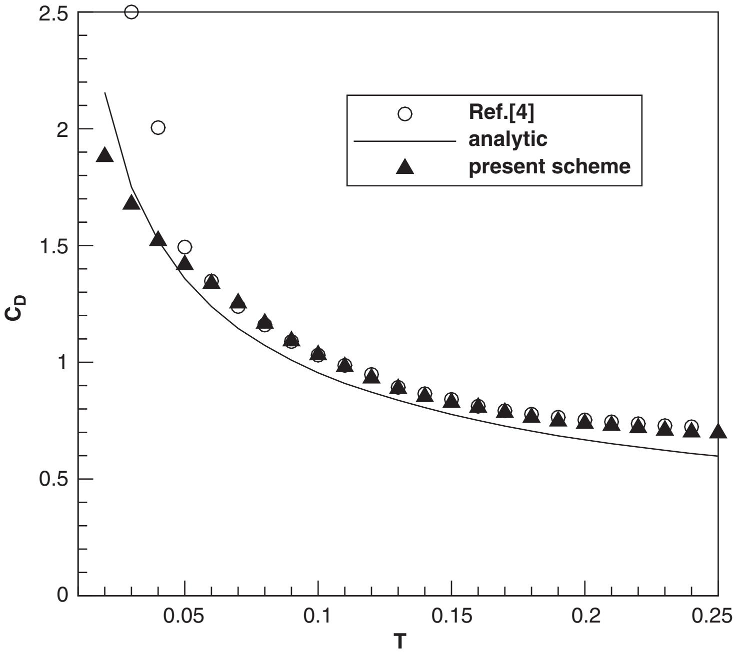

Figure 6. C_{D} comparison for the impulsively started cylinder problem $(0 < T < 0.25)$: solid line: solid line (–), analytical [20]; ▲, Lagrangian vortex method (present scheme); ○, Lagrangian vortex method [4].

This implies that the iterative process for the body boundary condition imposed in FVM is also applicable to the vortex particle method.

A comparison is made in Figure 4 of I_x as a function of $T = tU_\infty/D$ for the x-component of momentum $(\mathbf{I} = \int_\Omega \mathbf{x} \times \boldsymbol{\omega}\,\mathrm{d}s)$, $I_x = \int_\Omega y\omega\,\mathrm{d}\Omega = \sum_p y_p \Gamma_p$, and Figure 4 includes the analytical solution for early developing flows $(T < 0.25)$. The numerical and analytical results are in good agreement. As shown in Figure 5, for a longer time interval, the two numerical methods give indistinguishable results. The same comparison for the drag coefficient, $C_D = F_x/\frac{1}{2}\rho U_\infty^2 D$ with $F_x = -\rho\,\mathrm{d}I_x/\mathrm{d}t$, is shown in Figures 6 and 7. Here, the result obtained by FVM is included. Figure 6 shows that, of the two methods, the present Lagrangian scheme produces results somewhat closer to the analytical results.

Figure 8 represents the comparison of the body vorticity between the Eulerian FVM and the Lagrangian vortex method. The front stagnation point of the cylinder corresponds to the angular position of $\theta = \pi$ measured from the positive x-axis. The body vorticity obtained by the Lagrangian vortex method is the 'filtered' (smoothed) value. The Lagrangian scheme has high-frequency noise in the values due to dispersed particles, so the filtered value is taken by an inverse Fourier transformation of the 16 first modes. The agreement between the two methods is seen to be quite satisfactory, but with small differences at local extrema. It is observed that, as time progresses, the local peaks of body vorticity become large. These local peaks occur at the instant the vortical wake behind the cylinder develops.

Figure 9 shows the streamline patterns. It is found that the wake length behind the cylinder is half the diameter of the cylinder at $T = 2$, and almost the same as the diameter at $T = 4$.

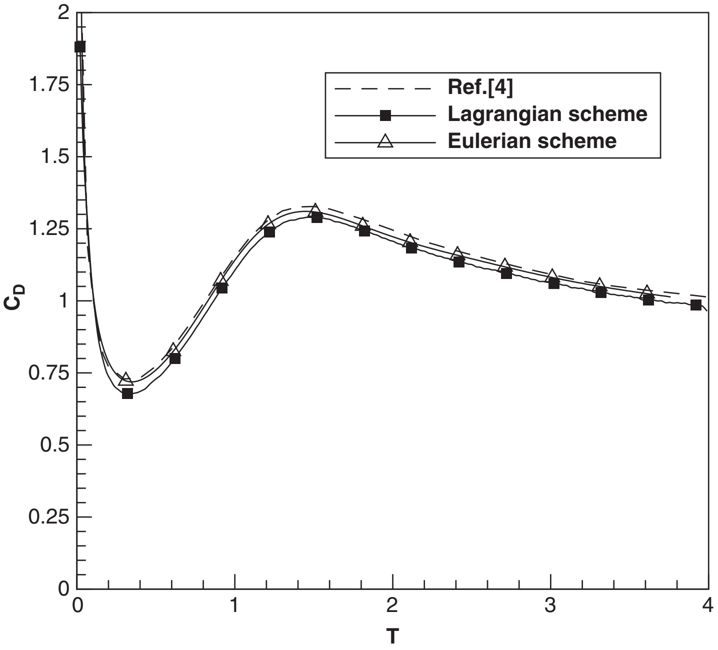

Figure 7. C_D comparison for the impulsively started cylinder problem ($0<T<4$): ■, Lagrangian vortex method; △, Eulerian FVM; dashed line (– –), Lagrangian vortex method [4].

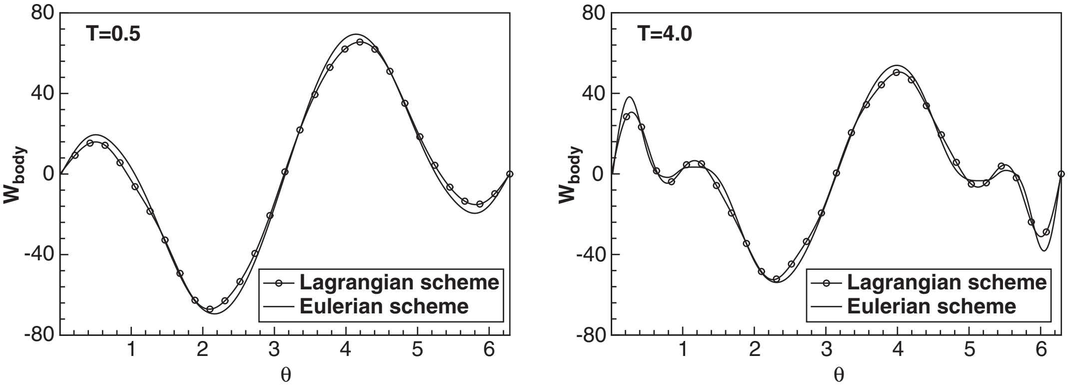

Figure 8. Body vorticity comparison for the impulsively started cylinder problem, $Re=550$ at $t=0.5$, $t=4.0$: solid line (–), Eulerian FVM; ○, Lagrangian vortex method.

At $T=2$, a secondary vortex is generated at a position of about $\theta=60°$. The results obtained from the Lagrangian vortex method and the Eulerian FVM are found to be almost identical, but the Lagrangian scheme produces short wavelength oscillations at regions where there are few nearby particles.

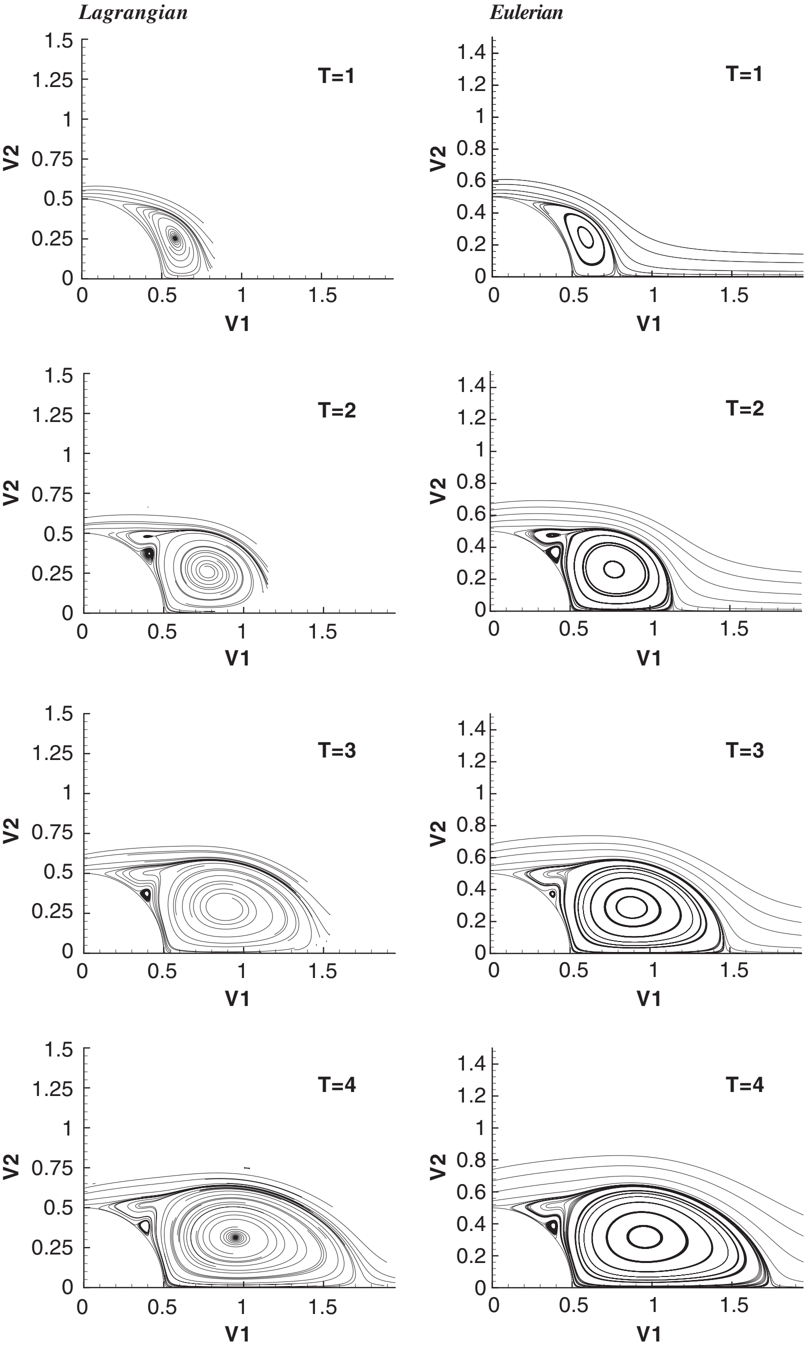

Figure 9. Streamline patterns for the impulsively started cylinder problem, $Re = 550$ at $T = 1$, $T = 2$, $T = 3$, $T = 4$: Lagrangian vortex method (left), Eulerian FVM (right).

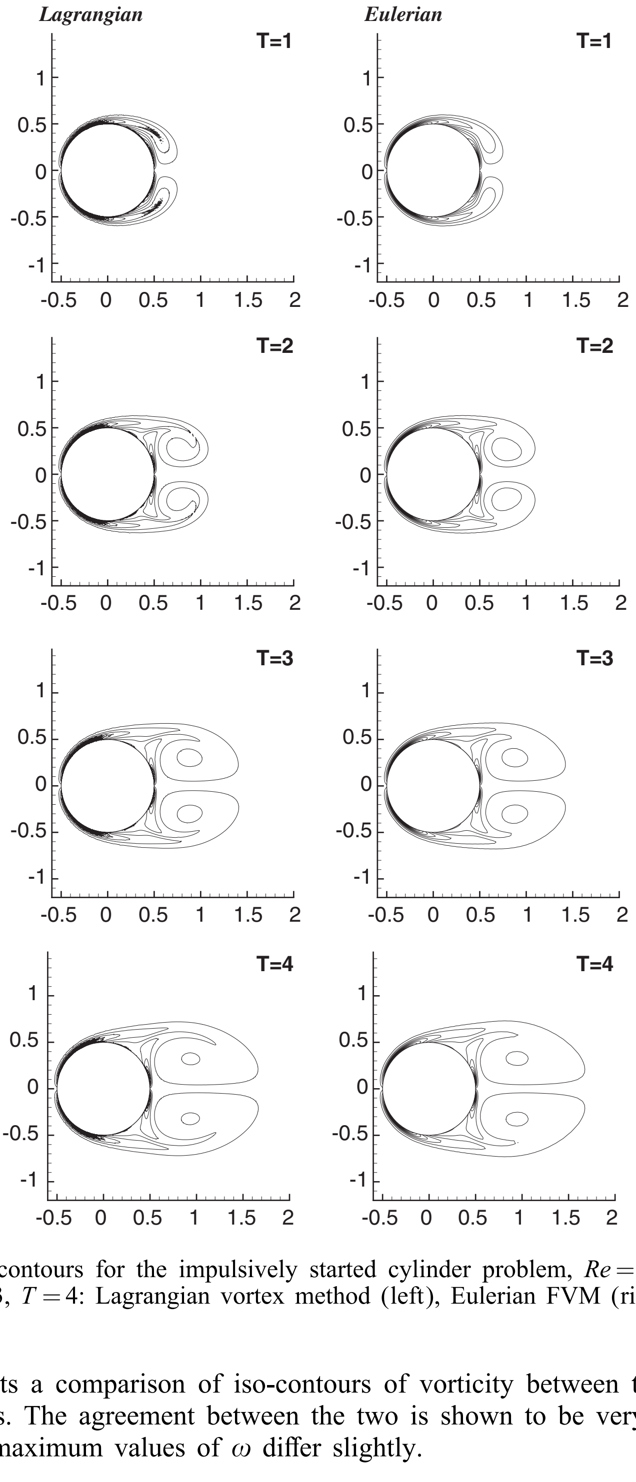

Figure 10. Vorticity contours for the impulsively started cylinder problem, $Re = 550$ at $T = 1$, $T = 2$, $T = 3$, $T = 4$: Lagrangian vortex method (left), Eulerian FVM (right).

Figure 10 presents a comparison of iso-contours of vorticity between the Lagrangian and Eulerian approaches. The agreement between the two is shown to be very good, except that the minimum and maximum values of ω differ slightly.

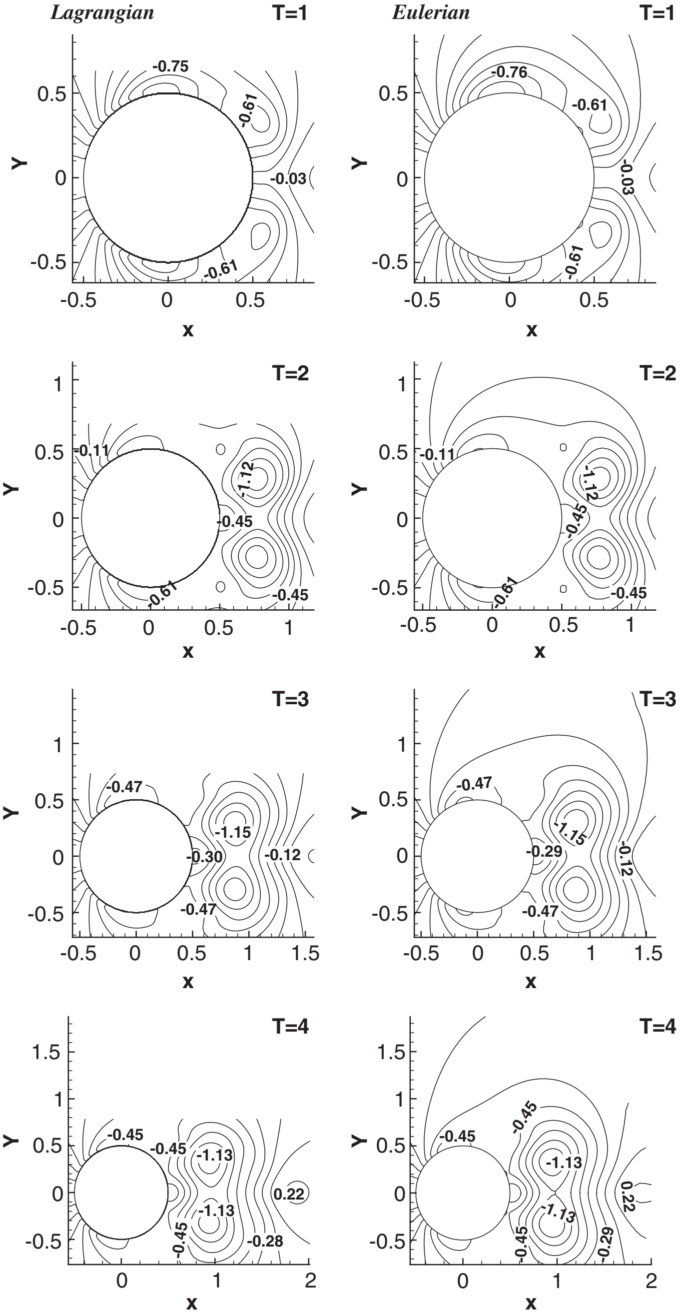

Figure 11. Pressure contours for the impulsively started cylinder problem, $Re = 550$ at $T = 1.0$, $T = 2.0$, $T = 3.0$, $T = 4.0$: Lagrangian vortex method (left), Eulerian FVM (right).

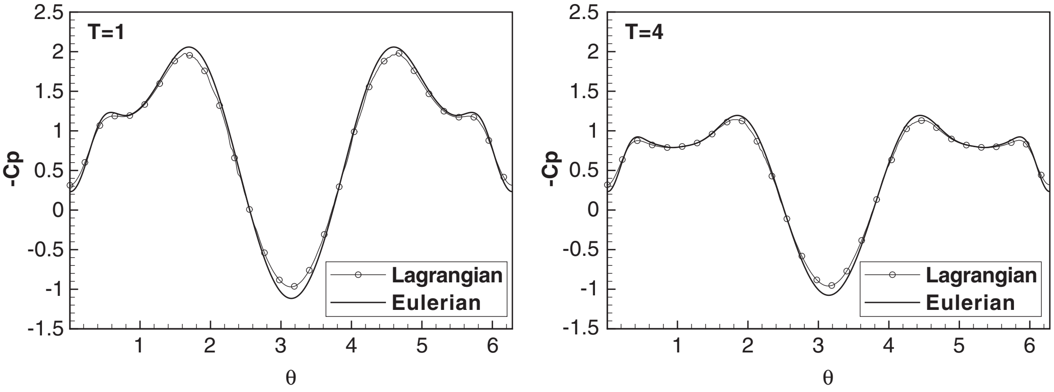

Figure 12. Comparison of C_p for the impulsively started cylinder problem, $Re = 550$ at $T = 1$, $T = 4.0$: solid line (−), Eulerian FVM; ○, Lagrangian vortex method.

Table II. Computational parameters for the impulsively started foil (NACA0021).

	Eulerian FVM	Lagrangian vortex method
Reynolds number	550	550
Time step, Δt	0.01	0.01
Thickness ratio	0.21	0.21
Number of surface panels	408	408
Angle of attack	5°,10°	5°,10°
Grid meshes	408 × 60	—
Particles	—	13 000–40 000
Computational domain	Chord × 3	No limit
Computational time	About 31 hours	About 50 hours
(Pentium IV)	(400 time steps)	(400 time steps)

Figure 11 shows the pressure contours in the computational domain. The results from the two methods are almost identical. As time advances, the pressure distributions are rapidly changed near strong vortical flow structures. It is seen that a low-pressure region is formed at the core of the downstream wake.

Figure 12 presents a comparison of pressure coefficients $C_p(=(p - p_\infty)/\rho u_\infty^2)$ on the body surface at several instants. It is observed that the agreement between these results is satisfactory. As time progresses, a region with a local peak develops. This is caused by the generation of the wake or vortex behind the circular cylinder.

4.2. Impulsively started foil with varying angles of attack

We now take the case of the impulsively started NACA0021 with varying angles of attack. The present image particle layer scheme is suitable for this case. The parameters used in the calculation are similar to the case of the impulsively started cylinder (see Table II).

The computing time is longer than in the case of the cylinder. The reason may be that the number of iterations required for canceling the spurious slip velocity and generating the

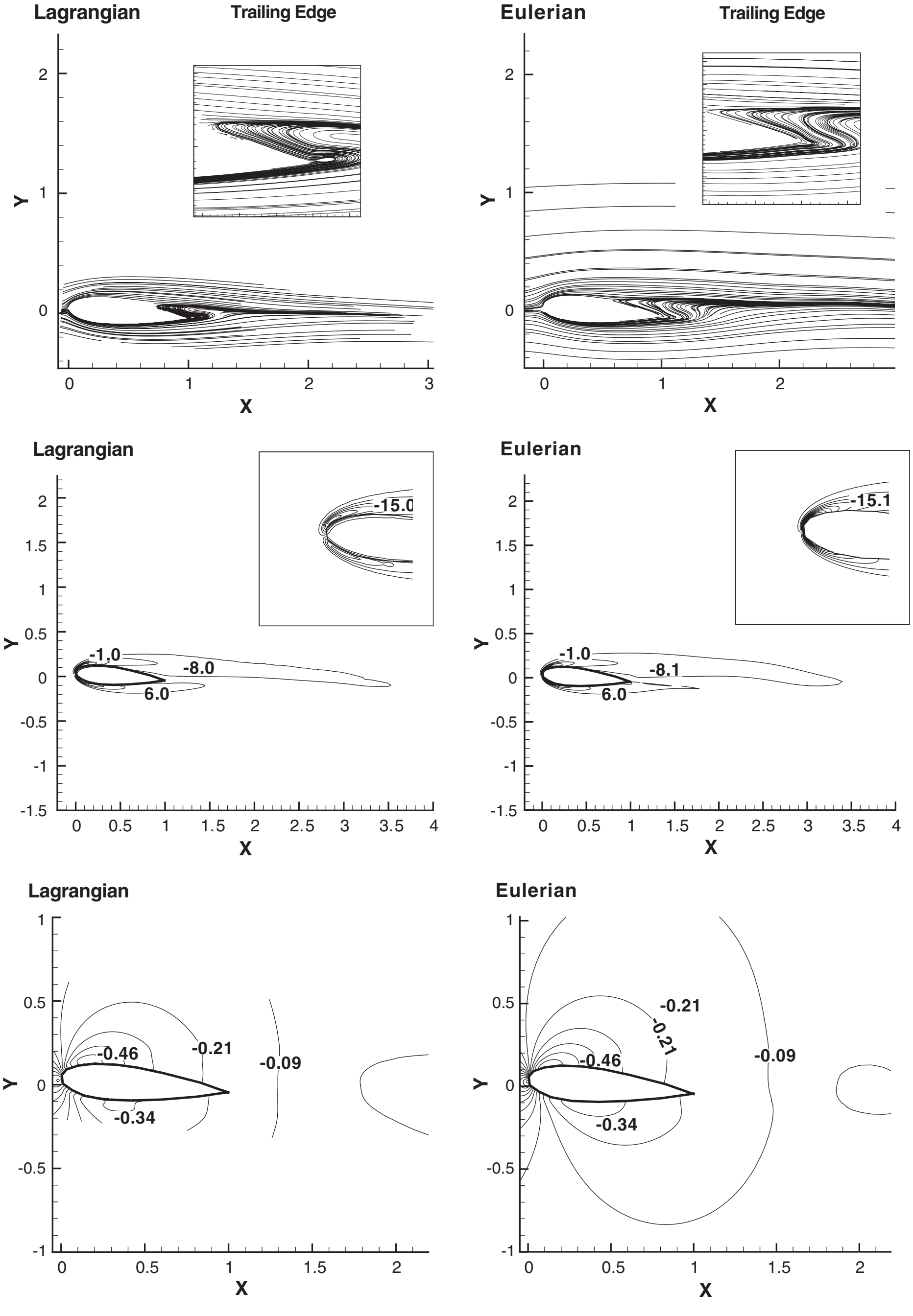

Figure 13. Streamline patterns, vorticity contours and pressure contours for the impulsively started NACA0021 foil, $Re = 550$ and $\alpha = 5^\circ$ at $T = 4.0$: Lagrangian vortex method (left), Eulerian FVM (right).

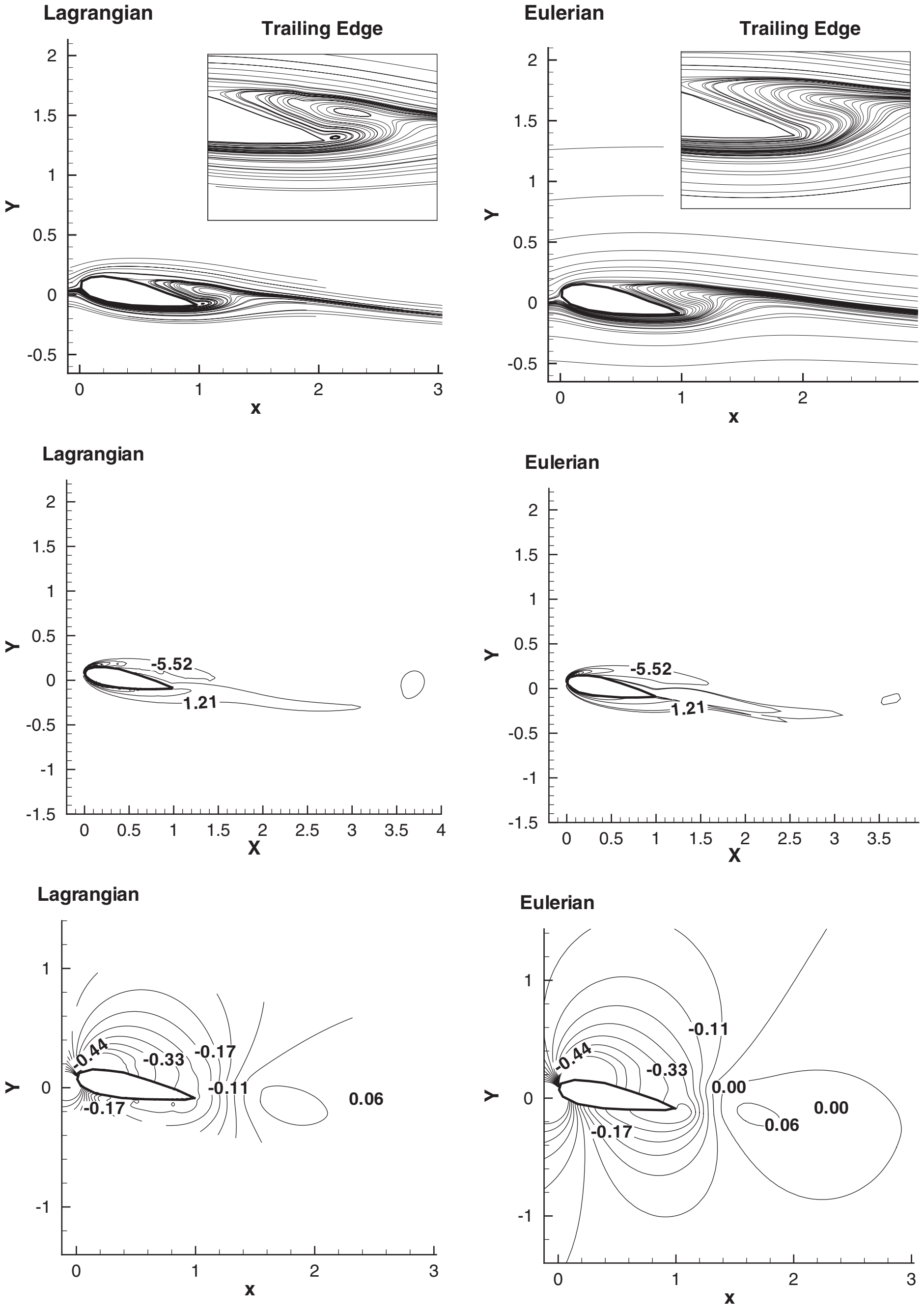

Figure 14. Streamline patterns, vorticity contours and pressure contours for the impulsively started NACA0021 foil, $Re = 550$ and $\alpha = 10^\circ$ at $T = 4.0$: Lagrangian vortex method (left), Eulerian FVM (right).

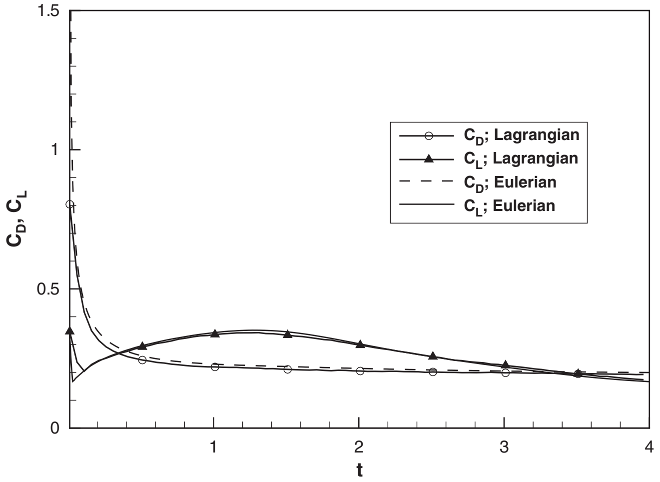

Figure 15. Drag and lift comparison for the impulsively started NACA0021 foil, $Re = 550$ and $\alpha = 5$: ○, C_D Lagrangian vortex method; ▲, C_L Lagrangian vortex method; dashed line (−−), C_D Eulerian FVM; solid line (−), C_L Eulerian FVM.

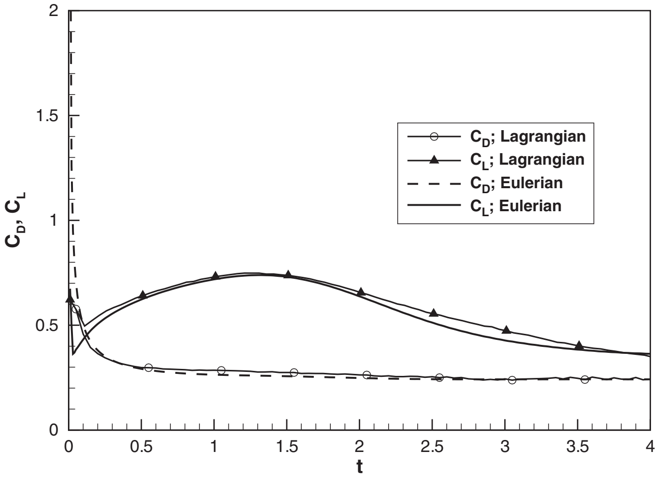

Figure 16. Drag and Lift comparison for the impulsively started NACA0021 foil, $Re = 550$ and $\alpha = 10$: ○, C_D Lagrangian vortex method; ▲, C_L Lagrangian vortex method; dashed line (−−), C_D Eulerian FVM; solid line (−), C_L Eulerian FVM.

vorticity flux on the body boundary is larger than that in the case of the cylinder problem. As the angle of attack is higher, the computing time is much longer. We applied the present scheme to the foil with two angles of attack, 5° and 10°.

Figure 13 shows the streamline patterns, the vorticity contours and pressure contours at Reynolds number 550 around the foil with angle of attack being 5°. The two results are shown to be in good agreement. In the streamline patterns, the reverse flows are captured near the trailing edge of the foil. As observed in the results of the Lagrangian vortex method, the fields of velocity and pressure are confined to the viscous region around the foil, because we consider only the field where the vorticity evolves and exists. Figure 14 shows the streamline patterns, the vorticity contours and pressure contours at Reynolds number of 550 at $T = 4.0$ for the angle of attack of 10°. This shows aspects similar to those of the previous case. Figures 15 and 16 show the comparison of the drag coefficients and the lift coefficients. In the case of angle of attack 5°, the results of Lagrangian vortex and Eulerian FVM methods are nearly identical. On the other hand, in the case of angle of attack 10°, there is a small difference between the results, especially at about $T = 3.0$. This may be due to the strong starting vortex. When the angle of attack of the foil is higher, the strength of the starting vortex is larger. Each scheme may reflect the evolution of the vorticity on the body in a different manner. In fact, we only focus on the unsteady flow simulation at an early stage. We may expect to obtain the same steady-state characteristics.

5. CONCLUDING REMARKS

This paper proposes a vorticity-based integro-differential formulation for the numerical solution of unsteady incompressible flows. The integral approach that is a fundamental part of the present formulation is directly applicable for solving the integral equation for the pressure field as well. The present scheme includes a pressure calculation which is a distinctive feature, not previously treated in most vorticity-based methods. These aspects have been adapted for the vorticity-velocity-pressure formulation by an Eulerian description.

For the kinematics of flow and the physical interpretation of the velocity field ($\mathbf{u} = \mathbf{u}_w + \nabla\phi + \mathbf{u}_\infty$), a Lagrangian vortex method connected with the panel method has been presented. An iterative process was used in order to enforce the no-slip condition through the vorticity flux at the body boundary. For a thin body, we suggest the use of an image particle layer for the zero-vorticity-flux condition on the solid boundary.

By applying the present scheme for the impulsively started cylinder and the impulsively started NACA0021 foil with angles of attack, we performed comparisons with existing results, and with the results of an Eulerian FVM.

Although the present work has mainly focused on comparative studies, future work would address the treatment of turbulence models, the extension of the vortex method to three-dimensional flow problems, and the development of efficient numerical schemes associated with the solution procedure.

ACKNOWLEDGEMENTS

This work was supported by the Ministry of Science and Technology (MOST), Korea under the projects (PN00630 & PN00690) and also supported by Korea Science and Engineering Foundation Grant (R11-2002-104-02002-0).

REFERENCES

1. Greengard L, Rokhlin V. A fast algorithm for particle simulations. *Journal of Computational Physics* 1987; **73**:325–348.

2. Degond P, Mas-Gallic S. The weighted particle method for convection diffusion equations. Part I: the case of an isotropic viscosity. Part II: the anisotropic case. *Mathematics of Computation* 1989; **53**:485–507.
3. Koumoutsakos PD, Leonard A, Pépin FM. Viscous boundary conditions for vortex methods. *Journal of Computational Physics* 1994; **113**:52–56.
4. Ploumhans P, Winckelmans GS. Vortex methods for high-resolution simulations of viscous flow past bluff bodies of general geometry. *Journal of Computational Physics* 2000; **65**:354–406.
5. Ploumhans P, Winckelmans GS, Salmon JK, Leonard A, Warren MS. Vortex methods for direct numerical simulation of three-dimensional bluff body flows: application to the sphere at $Re = 300, 500$, and 1000. *Journal of Computational Physics* 2002; **178**:427–463.
6. Leonard A. Vortex methods for flow simulation. *Journal of Computational Physics* 1980; **37**:289–335.
7. Pépin FM. Simulation of the flow past an impulsively started cylinder using a discrete vortex method. *Ph.D. Thesis*, California Institute of Technology, U.S.A., 1990.
8. Koumoutsakos PD. Direct numerical simulations of unsteady separated flows using vortex methods. *Ph.D. Thesis*, California Institute of Technology, U.S.A., 1993.
9. Ying L-A, Zhang P-W. *Vortex Methods*. Science Press and Kluwer Academic Publisher: Beijing, 1997.
10. Cottet G-H, Koumoutsakos PD. *Vortex Methods*: *Theory and Practice*. Cambridge University Press: Cambridge, 2000.
11. Wu JC. Numerical boundary conditions for viscous flow problems. *AIAA Journal* 1976; **14**(8):1042–1049.
12. Gresho PM. Incompressible fluid dynamics: some fundamental formulation issues. *Annual Review of Fluid Mechanics* 1991; **17**:411–445.
13. Wu J-Z, Wu X-H, Ma H-Y, Wu J-M. Dynamic vorticity condition: theoretical analysis and numerical implementation. *International Journal for Numerical Methods in Fluids* 1994; **19**:905–938.
14. Koumoutsakos PD, Leonard A. High-resolution simulations of the flow around an impulsively started cylinder using vortex methods. *Journal of Fluid Mechanics* 1995; **296**:1–38.
15. Suh J-C, Kim K-S. A vorticity-velocity formulation for solving the two-dimensional Navier–Stokes equations. *Fluid Dynamics Research* 1999; **25**(4):195–216.
16. Morino L. Helmholtz and Poincare potential-vorticity decompositions for the analysis of unsteady compressible viscous flows. In *Boundary Element Methods in Nonlinear Fluid Dynamics*, Banerjee PK, Morino L (eds). Elsevier Applied Science: London, New York, 1990; 1–54.
17. Lee J-T. A potential based panel method for the analysis of marine propellers in steady flow. *Ph.D. Thesis*, M.I.T., U.S.A., 1987.
18. Suh J-C, Lee J-T, Suh S-B. A bilinear source and doublet distribution over a planar panel and its applications to surface panel methods. *Proceedings of the Nineteenth Symposium on Naval Hydrodynamics*, 1992; 102–112.
19. Kim K-S. A vorticity-velocity-pressure formulation for numerical solutions of the incompressible Navier–Stokes equation. *Ph.D. Thesis*, Seoul National University, Korea, 2003.
20. Bar-Lev M, Yang HT. Initial flow field over an impulsively started circular cylinder. *Journal of Fluid Mechanics* 1975; **72**:625–647.
21. Lighthill MJ. Introduction, boundary layer theory. In *Laminar Boundary Layers*, Rosenhead J (ed.). Oxford University Press: New York, 1963; 54–61.
22. Wu J-Z, Wu J-M. Interactions between a solid surface and viscous compressible flow field. *Journal of Fluid Mechanics* 1993; **254**:183–211.
23. Suh J-C. The evaluation of the Biot–Savart integral. *Journal of Engineering Mathematics* 2000; **37**:375–395.
24. Winckelmans G, Leonard A. Improved methods for three-dimensional flows. In *Mathematical Aspects of Vortex Dynamics*, Caflish R (ed.). SIAM: Philadelphia, PA, 1989; 25–35.
25. Winckelmans G, Leonard A. Contributions to vortex particle methods for the computation of three-dimensional incompressible unsteady flows. *Journal of Computational Physics* 1993; **109**:247–273.
26. Loc TP, Bouard R. Numerical solution of the early stage of the unsteady viscous flow around a circular cylinder: a comparison with experimental visualization and measurements. *Journal of Fluid Mechanics* 1985; **160**:93–117.
27. Batchelor GK. *An Introduction to Fluid Dynamics*. Cambridge University Press: Cambridge, 1967.